nature communications

Article

https://doi.org/10.1038/s41467-025-57652-6

Pinpointing the thermal history of lunar basaltic meteorites in a nutshell

Received: 23 July 2024

Accepted: 27 February 2025

Published online: 01 May 2025

Check for updates

Pierre Vonlanthen[1] ✉, Farhang Nabiei[2,3,6], Cyril Cayron[4], A. Brian Aebersold[2,7], Martin Robyr[1], Mary-Alix Kaczmarek[5], Othmar Müntener[1] & Philippe Gillet[3]

Native metals of igneous origin are recognized as one of the distinctive features of basalts from the Moon. Our study demonstrates that the tiny Fe-Ni metal blebs nucleated from lunar magma exhibit unanticipated, nutshell-like, crystallographic microstructures, that can be used in conjunction with local variations in chemical compositions to trace the complete thermal history of the host rock. This encompasses rapid cooling on the lunar surface, shock reheating upon impact, and post-shock cooling in the outer space. The Fe-Ni metal blebs indicate that the lava cooled in two stages, first down to 90–160 °C during lunar daytime, and then, to −160 °C during nighttime. Upon shock, the (near-)equilibrium peak temperature of 660–690 °C was reached shortly after release to zero pressure, mainly by thermal conduction from hot vesicular plagioclase. Here, we show that intense shock heating is compatible with the small impact scenario put forward for lunar meteorites and that metals are pioneering full-range geothermometers capable of tracing the complete thermal history of achondritic planetary materials.

Fe-Ni alloys of extraterrestrial origin have been the subject of extensive scrutiny over the last decades, to gain insight into the evolution of the early solar system[1–6]. The majority of these studies have focused on iron and iron-rich meteorites cooled at extremely low rates and under near-equilibrium conditions. The goal was to better constrain the phase boundaries and the stability fields of the Fe-Ni phase diagram. At the opposite end of the spectrum, the thermal history of stony meteorites, such as the planetary and asteroidal achondrites, has been deciphered from very different geothermometers, based either on the partitioning of chemical elements or isotopes between co-existing silicate minerals[7,8], or on the site occupancy of specific atoms within the crystal lattice[9]. While these geothermometers have proven effective in determining the closure temperatures in near-equilibrium systems with well-known diffusion rates and partition coefficients, they have shown significant limitations when applied to shocked rocks, i.e., extremely chaotic systems in which nearly instantaneous and highly heterogeneous heating upon impact is the norm. Moreover, since standard geothermometers are dependent on the diffusion of chemical elements, which limits their use below closure temperatures, they are unable to record the cold stages of rock history.

To address the potential of Fe-Ni metal blebs as geothermometers for achondritic rocks, we investigated a subsample of meteorite NWA 479, an exceptionally fresh and unbrecciated mare basalt[10] paired with meteorite NWA 032[11,12]. Meteorite NWA 479 exhibits large phenocrysts of chromite, olivine, and pyroxene, within a fine-grained groundmass of intergrown pyroxene and plagioclase[10] (see Supplementary Section 1). The dating indicates a crystallization age of 2.8 Ga[13–15] and an ejection age of ~50 ka[16,17] (Moon-Earth transfer plus terrestrial residence time).

[1]Institute of Earth Sciences, University of Lausanne, Lausanne, Switzerland. [2]Interdisciplinary Centre for Electron Microscopy, Ecole Polytechnique Fédérale de Lausanne, Lausanne, Switzerland. [3]Institute of Physics, Ecole Polytechnique Fédérale de Lausanne, Lausanne, Switzerland. [4]Institute of Materials, Ecole Polytechnique Fédérale de Lausanne, Lausanne, Switzerland. [5]Geosciences Environment Toulouse, University of Toulouse, Toulouse, France. [6]Present address: Mediatek Research, Cambourne Business Park, Cambridge, United Kingdom. [7]Present address: Sensirion AG, Stäfa, Switzerland.
✉e-mail: pierre.vonlanthen@unil.ch

Here, we show that the complete thermal history of lunar meteorites can be elucidated in detail, encompassing processes such as igneous cooling and shock reheating upon impact, as well as post-shock cooling in the outer space. The analysis of sub-microstructural features and chemical compositions retrieved from the Fe-Ni metal blebs, in conjunction with a refined version of the T-$X_{Fe,Ni}$ phase diagram, indicates that high equilibrium peak-shock temperatures are compatible with a small impact scenario involving a shallow ejection depth from a small crater excavated by a moderately energetic impactor.

Results and discussion

Nutshell-like microstructure of Fe-Ni metal blebs

The Fe-Ni metals in meteorite NWA 479 form elliptical to sub-rounded blebs, with a diameter ranging between 5 and 30 µm. Most of them are located within the igneous groundmass, in direct contact with large euhedral chromite, or, in a few instances, as inclusions within olivine phenocrysts (Fig. S2). These features indicate that nucleation and growth occurred at depth, at an early stage in the crystallization sequence of the magma (see Supplementary Section 1). The Fe-Ni metal blebs studied here should not be confused with those of meteoric origin that have been frequently reported in the lunar regolith[18,19].

The apparent homogeneity of the Fe-Ni metal blebs in standard field emission-scanning electron microscope (FE-SEM) backscattered electron (BSE) images is challenged by electron backscatter diffraction (EBSD) crystallographic orientation maps, which reveal a previously unknown, core-rim, microstructure, surprisingly reminiscent of a nut nestled within its shell (Fig. 1a). The cores of the Fe-Ni metal blebs are polycrystalline and primarily composed of sub-µm to µm-sized, twinned, and rather lath-shaped body-centered cubic (hereafter bcc) grains, along with tiny interstitial face-centered cubic (hereafter fcc) grains. The cores are typically encased in a single-crystal fcc rim that exhibits smooth and gradual misorientations of up to ~50°, which suggests that the material was deformed under a plastic regime. The sporadic occurrence of sharper misorientations across (sometimes concentric) fractures indicates that the rim was also subject to moderate semi-brittle deformation. The recrystallization of the rim into twinned and deformation-free fcc grains is uncommon and occurs only on a local scale. The Fe-Ni metal blebs with a thin fcc rim (less than

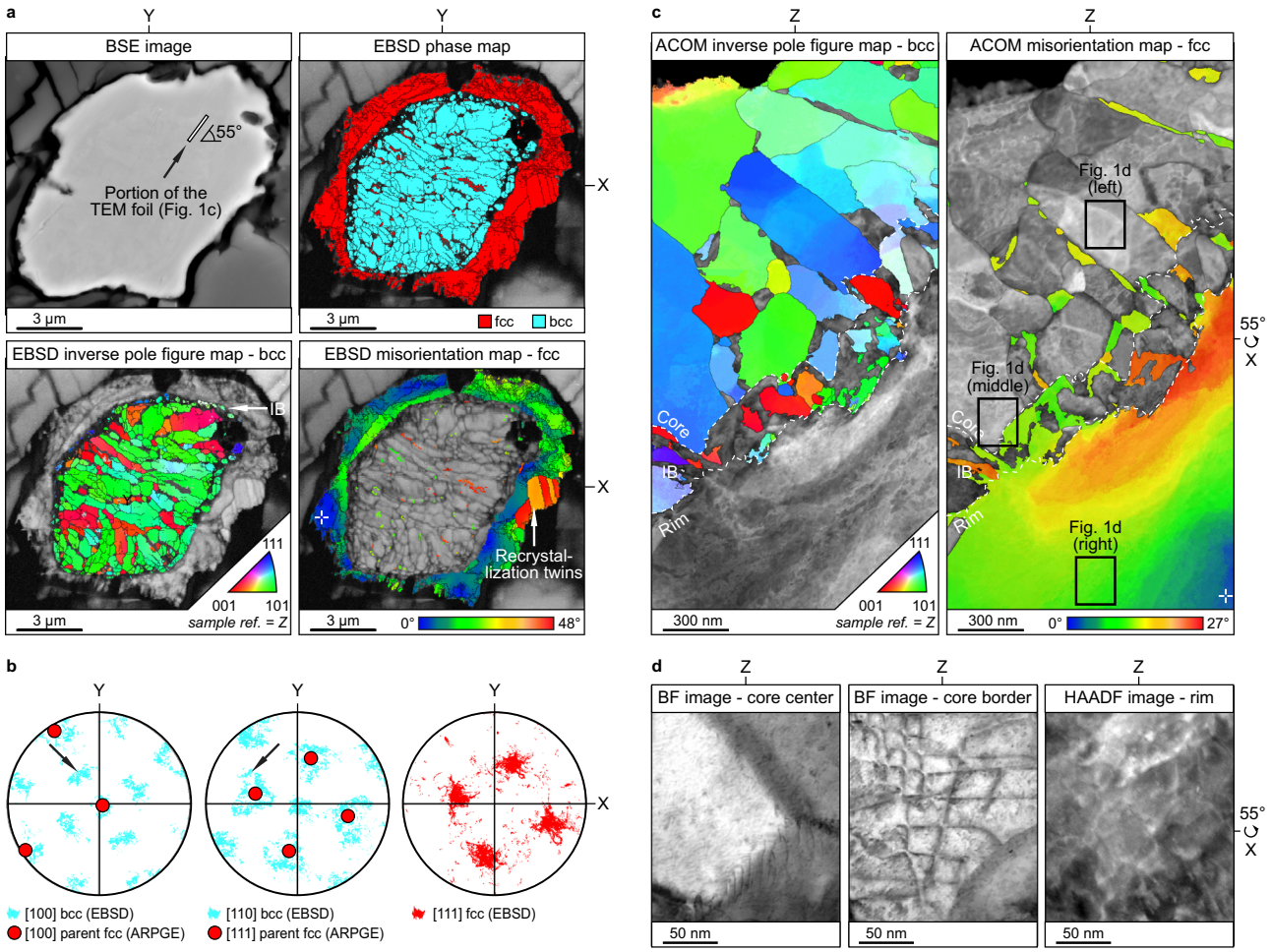

Fig. 1 | Typical nutshell-like microstructure of a solid Fe-Ni metal bleb. a SEM BSE image and EBSD maps showing the polycrystalline bcc core (with interstitial fcc grains) encased in the single-crystal, plastically deformed, fcc rim. A thin intermediate band (IB) made of tiny bcc and fcc grains is evident between the core and the rim. The grayscale background images are based on the band contrast of EBSD patterns. **b** Upper hemisphere stereographic pole figures of the measured bcc and fcc orientations for the bleb shown in (**a**), compared with the crystallographic orientation of the parent fcc grain (red discs) calculated using the ARPGE software[24]. The overlap of the measured and calculated [111] fcc axes indicates that the bcc grains have formed from a single fcc crystal having the orientation of the present rim. Examples of bow tie patterns and threefold stars are indicated by arrows (see other texts[112] for comparison). **c** Ultra-high resolution TEM ACOM maps showing the crystallographic orientations of the bcc grains in the core and the intermediate band (left), as well as the orientation shared by the retained interstitial fcc grains from the core and the intermediate band, and the plastically deformed fcc rim (right). The grayscale background images reflect the reliability of the TEM diffraction pattern indexing. **d** STEM bright-field (BF) and high-angle annular dark-field (HAADF) images of the dislocation substructures in the areas framed in (**c**). A comprehensive and detailed compilation of analogous data collected from the seven blebs investigated in this study can be found in Figs. S3–S5.

one-third of the bleb radius) show a structurally chaotic intermediate band, up to 0.3 µm in thickness, between the core and the rim (Fig. 1a, and blebs 2 and 6 in Figs. S3 and S4, respectively). The intermediate band is made of tiny bcc and fcc grains, measuring between 0.1 and 0.3 µm. These are approximately one order of magnitude smaller than the bcc grains observed in the core, and no clear crystallographic preferred orientations could be identified. No intermediate band was observed in blebs with a thick fcc rim (bleb 3 in Fig. S3, and blebs 4 and 5 in Fig. S4). The different mechanical behavior of the fcc rims and bcc cores, with the prevalence of pervasive plastic deformation in the former and the near absence thereof in the latter, can be attributed to the lower critical resolved shear stress (CRSS) of the fcc lattice than the bcc one[20–22], and the massive decrease in ductility with grain size[23].

Parent grain identification using the ARPGE software[24] indicates that the bcc grains in the core have originated from a single fcc crystal having the orientation of the present rim (Fig. 1b and Figs. S3–S5). The preferred distribution of poles for bcc grains, with clusters forming threefold stars and bow tie patterns, typically reflects the Kurdjumov-Sachs[25] and Nishiyama-Wassermann[26,27] inter-grain orientation relationships widely reported for fcc-to-bcc transformations in steels. Ultra-high resolution crystallographic orientation mapping (ACOM) in the field emission-transmission electron microscope (FE-TEM) indicates that the fcc rim exhibits similar crystallographic orientations to the majority of the interstitial fcc grains present in the core and the intermediate band (Fig. 1c). This suggests that these grains have been retained after incomplete transformation of the parent fcc single crystal.

Distinct dislocation substructures are present from the core to the rim (Fig. 1d). In the core center, regular planar arrays of dislocations form subgrain boundary walls meeting at triple junctions, while in the core outer border, most grains show straight and parallel dislocations crossing at right angles. The rim is characterized by a poorly defined, cell-like, structure delimited by a network of dislocations exhibiting varying degrees of density and entanglement. In the intermediate band, the dislocation distribution is chaotic, though obtaining a definitive picture of it is hindered by the tiny size of the grains (i.e., significantly smaller than the thickness of the TEM foil).

Cavities of up to several micrometers in diameter and well-documented in the metallurgical literature as Kirkendall voids[28] have been observed in the core of some Fe-Ni metal blebs. In many cases, these coalesce to form a single, larger cavity, resulting in hollow blebs that are suggestive of nut-free shells. Hollow Fe-Ni metal blebs typically exhibit the smallest bcc grains, with a size of <1 µm. No systematic correlation has been identified between the nature (hollow or solid) of the blebs, and the occurrence of an intermediate band between the core and the rim. In contrast to the solid blebs, however, the hollow ones are commonly filled or lined with Fe-Ni-rich (>50 vol%) glass, which occasionally spreads outwards to form a distinct layer between the bleb and the surrounding phases (Fig. 2a). The interface between the Fe-Ni metal and the Fe-Ni-rich glass is uneven and often propagates within the bleb rim to form strings of globular melting features or more sizable clusters (Fig. 2b). The Fe-Ni-rich glass itself is devoid of vesicles, though it is sometimes fractured. Despite the wealth of information they provide, the hollow blebs have been deemed ineligible as thermal indicators, particularly during the shock pulse (see Supplementary Section 2).

Additionally, porosity occurs in the form of contraction gaps, measuring between 0.05 and 0.5 µm in thickness, between the Fe-Ni metal blebs and the surrounding basalt (Fig. 1a and Figs. S3–S5). The formation of contraction gaps is attributed to the pronounced shrinkage of Fe-Ni metals on cooling, which is in line with their high thermal expansion coefficients (except below 100 °C for alloys with an Invar composition) compared to those of the surrounding minerals[29–31].

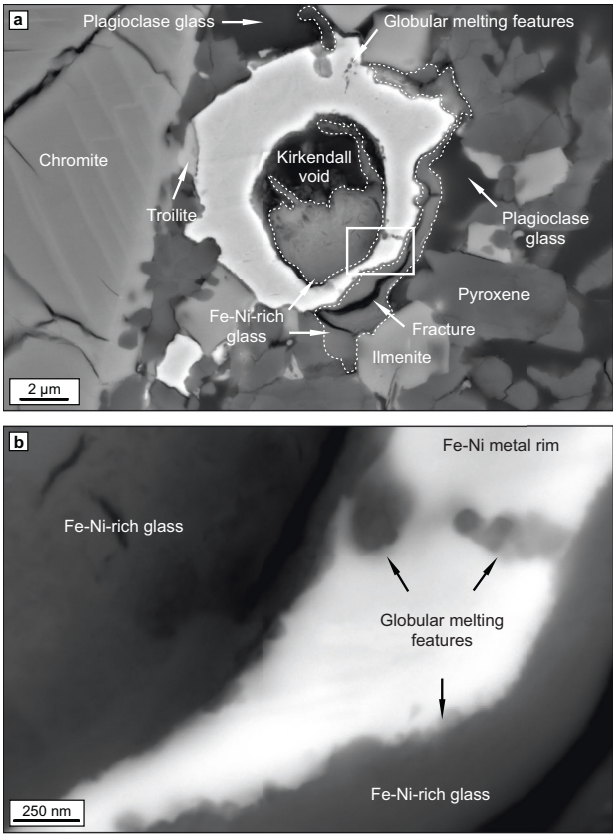

Fig. 2 | SEM BSE images of a hollow Fe-Ni metal bleb. a Fe-Ni-rich glass (dotted lines) located between the outer border of the rim and the nearby phases (mostly plagioclase glass), and within the free space left by the large internal cavity. **b** Close-up view of the square shown in (**a**) focusing on the globular melting features within the rim and at the interface between the rim and the Fe-Ni-rich glass (see also Fig. S4).

Other noteworthy characteristics not previously documented in earlier petrographic descriptions of meteorites NWA 479 and NWA 032 include the widespread vesiculation of plagioclase glass, overpressure cracks linking pairs of vesicles nucleated on either side of pyroxene grains, and Si-rich liquids forming mushroom-shaped or rounded blobs that are immiscible with plagioclase glass. Local melting of refractory phases occurs, including ilmenite (which should be distinguished from the ilmenite dendrites grown on igneous cooling) and pyroxene in contact with the plagioclase glass (Figs. 3 and S6). All these features are observed throughout the rock, at distances of up to hundreds of micrometers away from shock melt veins or pockets, which precludes the possibility of formation through friction heating.

An abrupt step disrupting the smooth core-to-rim chemical zoning

Energy-dispersive X-ray spectroscopy (TEM-EDS) maps and profiles performed in bleb 1 (Fig. 4a) indicate chemical zoning, with a gradual decrease in Fe and a corresponding increase in Ni (and Co) from the core to the rim. The strength of this gradient is not constant along the bleb radius, exhibiting a steeper slope in the inner portion of the rim than in the core center and the external portion of the rim. In addition to this long-range (µm-scale) core-to-rim zoning, the bcc grains of the core display a short-range (nm-scale) depletion of Ni towards grain boundaries, while interstitial fcc grains are noticeably enriched in Ni (Fig. 4b). Importantly, an unusually abrupt change in chemical composition occurs across the interface between the core and the intermediate band, i.e., with values for the bcc grains jumping from 77.6 wt% Fe,

https://doi.org/10.1038/s41467-025-57652-6

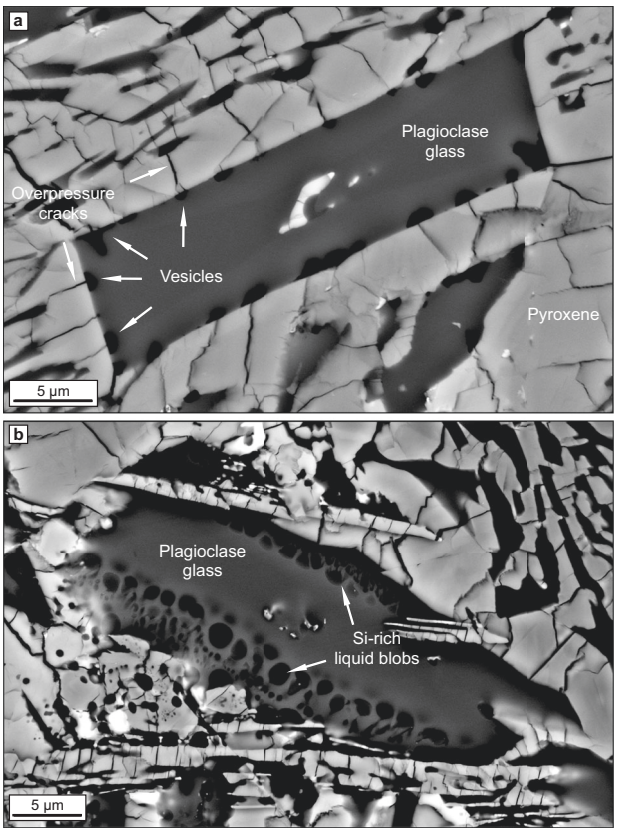

Fig. 3 | SEM BSE images showing evidence for plagioclase melting. a Vesicular plagioclase glass preserving the idiomorphic shape of the parent crystal. Vesicles are associated with overpressure cracks in neighboring pyroxene. **b** Mushroom-shaped and rounded Si-rich liquid blobs immiscible with plagioclase glass. An extended version (Fig. S6) can be found in Supplementary Section 3 (which also includes a discussion of the influence of these features on the equilibrium peak-shock pressure estimates reported in the literature).

19.3 wt% Ni, 3.2 wt% Co to 74.0 wt% Fe, 22.7 wt% Ni, 3.4 wt% Co, respectively (see Table S1). No such prominent compositional step has been observed across the intermediate band and the rim, with a composition on either side of the interface of ~67.8 wt% Fe, ~28.6 wt% Ni, and ~3.6 wt% Co.

The chemical compositions obtained from in-situ analyses of seven Fe-Ni metal blebs (Table 1) using wavelength-dispersive X-ray spectroscopy (WDS) are in good agreement with the TEM-EDS data of bleb 1, indicating that core-to-rim zoning is a common trait across all blebs of lunar meteorite NWA 479. A correlation is observed between the thickness of the rim and the occurrence of an intermediate band on the one hand, and the composition of the outer border of the rim on the other hand. The Fe-Ni metal blebs with a thin fcc rim and an intermediate band consistently show $(Fe/Ni)_{rim}$ ratios greater than 1.2, whereas those with a thick fcc rim and no discernible intermediate band are below this value. It is hypothesized that the flatter core-to-rim zoning profiles observed in the former allow for sufficient resolution of the intermediate band by EBSD. However, this assertion cannot be fully verified due to the variable accessibility of the core centers for WDS chemical measurements (peripheral sectioning, absence of a core center in hollow blebs), or the fortuitous incorporation of shallow interstitial Ni-rich fcc grains within the X-ray emission volume. Furthermore, WDS analyses indicate that the total concentration of the trace and minor elements P, Cr, S, F, Cl, Ti, Si, and Ca is consistently below 1.5 wt%. The most abundant of these elements is Cr, with concentrations of 0.50–0.99 wt% in the cores, and 0.25–0.64 wt% in the outermost portions of the rims (with the exception of bleb 7, which grew at a distance from chromite; see Table 1 and Fig. S5). As is the case with any lunar basalts containing native metals, the carbon content is expected to be extremely low. This is in accordance with the strong reduction of the magma at depth, which involved the scavenging of oxygen to form carbon monoxide and dioxide at an early stage of the igneous history[32,33].

Towards a new geothermometer for lunar basalts

The complete thermal history of meteorite NWA 479, illustrated in the T-$X_{Fe,Ni}$ phase diagrams of Fig. 5, was retrieved from the coupling of the sub-microstructures and the chemical compositions of the Fe-Ni metal blebs with the temperatures of the fcc-to-bcc (martensitic) and bcc-to-fcc (austenitic) finish transformation curves (labeled M_F and A_F). The methodology used to refine the position and shape of M_F and A_F (originally established at ambient pressure and for binary, coarse-grained, Fe-Ni alloys[34]), with the microstructural and chemical attributes of the Fe-Ni metals blebs studied here is detailed in Supplementary Section 4. In brief, we show that the modifications and shifts that must be applied to the key points in the M_F and A_F curves are primarily influenced by the presence of alloying elements, with a minor contribution from the grain size in the inner portion of the

Table 1 | WDS chemical compositions (wt%) of the seven Fe-Ni metal blebs identified in the subsample of meteorite NWA 479

	Fe-Ni metal blebs													
	1[a]		2		3[a]		4		5		6		7[b]	
	Core	Rim	Core	Rim	Core	Rim	Core	Rim	Core	Rim	Core	Rim	Core	Rim
Fe	86.00	54.40	84.65	60.06	65.00	51.60	78.86	50.71	82.01	48.23	78.29	58.81	87.03	68.86
Ni	12.00	41.50	12.30	33.18	31.80	44.40	17.17	42.95	15.03	46.19	17.19	34.08	11.28	26.54
Co	2.00	4.10	1.35	3.12	3.20	4.00	1.48	2.78	1.44	2.56	1.53	2.84	1.34	2.64
P	nd	nd	0.01	<0.01	nd	nd	<0.01	<0.01	0.01	<0.01	<0.01	0.01	0.02	0.01
Cr	nd	nd	0.82	0.44	nd	nd	0.50	0.27	0.51	0.25	0.99	0.71	0.07	0.08
F	nd	nd	<0.01	0.01	nd	nd	<0.01	0.06	<0.01	0.05	<0.01	0.03	<0.01	0.04
Si	nd	nd	0.04	0.05	nd	nd	0.05	0.07	0.14	0.04	0.06	0.07	0.03	0.06
Ca	nd	nd	0.13	0.19	nd	nd	0.14	0.18	0.17	0.12	0.16	0.20	0.12	0.19
Ti	nd	nd	0.15	0.13	nd	nd	0.15	0.21	0.19	0.21	0.21	0.25	0.05	0.10
S	nd	nd	<0.01	0.01	nd	nd	<0.01	<0.01	0.01	0.01	0.01	0.01	<0.01	<0.01
Cl	nd	nd	<0.01	<0.01	nd	nd	<0.01	<0.01	<0.01	<0.01	<0.01	<0.01	0.01	<0.01
Total	100.00	100.00	99.45	97.20	100.00	100.00	98.35	97.22	99.50	97.66	98.44	97.01	99.94	98.50
Fe/Ni	7.17	1.31	6.88	1.81	2.04	1.16	4.59	1.18	5.46	1.04	4.55	1.73	7.72	2.59

The locations of the analyses are indicated by white discs in the EBSD phase maps of Figs. S3–S5. The Fe/Ni ratios of the core (centers) should be regarded as lower bounds (see text for discussion).
[a]Values retrieved from the (standardless) quantitative EDS measurements, as these blebs did not survive the (destructive) FIB/TEM sample preparation; nd is for no data. Bleb 1 is illustrated in Figs. 1 and 4, and bleb 5 in Fig. 2. A compilation of the seven blebs is illustrated in Figs. S3–S5.
[b]Bleb with no fcc, but a microgranular, fcc-bcc composite rim.

https://doi.org/10.1038/s41467-025-57652-6

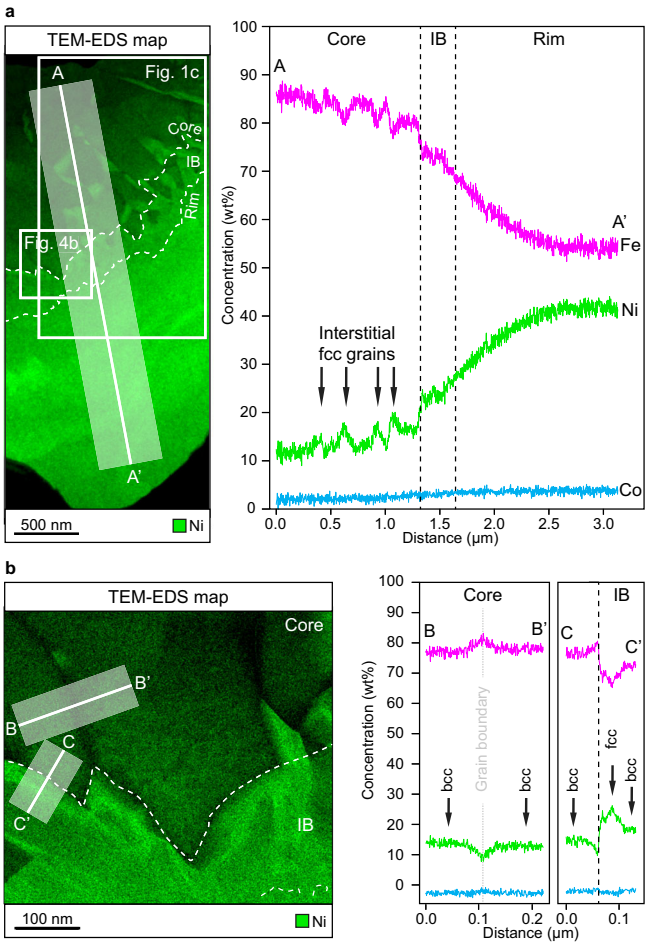

Fig. 4 | Chemical distribution of Fe/Ni/Co. a TEM-EDS (Kα) Ni map and Fe/Ni/Co profiles (AA') of the bleb shown in Fig. 1 illustrating the smooth compositional gradient from the core to the rim, disrupted only by retained fcc grains and the abrupt step between the core and the intermediate band (IB). The large white frame indicates the location of Fig. 1c. **b** Close-up Ni map and Fe/Ni/Co profiles showing the concentrations across the interface between two bcc grains of the core (BB'), and across the core and the intermediate band (CC').

intermediate band. Conversely, the initial particle size and the compression regime induced by (largely relaxed) differential volumetric changes have a negligible effect on M_F and A_F.

The question of whether the transformations should be better designated as martensitic or bainitic is not crucial in this context, first because martensite and bainite start (and finish) temperature curves are equivalent for Fe-Ni alloys containing more than 5 wt% Ni[35], and then because some ambiguity still persists between the dominant schools of thought[36] regarding the nomenclature to be used in the phase transformations of carbon-free or -poor Fe-Ni metals. For the sake of simplicity, the transformations were named simply as fcc-to-bcc (or bcc-to-fcc in the case of back transformations, also referred to as reverse or austenitic). A general explanation of martensitic transformations can be found in Supplementary Section 4.

Igneous origin of core-to-rim Fe-Ni zoning

During the initial, high-temperature (~1500 °C), stage of cooling, the chemical composition of the blebs was homogeneous, with constant Fe/Ni (and Fe/Co) ratios from the core to the rim. As the temperature decreased, the growth of chromite phenocrysts resulted in a notable depletion of Fe in the melt. A chemical gradient developed between the Fe-rich metal blebs and the comparatively Fe-poor melt, resulting in the diffusion of Fe from the blebs towards the melt and the formation of the long-range core-to-rim zoning still visible today. Alternatively, the loss of Fe from the rim of the blebs may also have been facilitated by a shift of the melt towards more oxidizing conditions during fractional crystallization, as reported elsewhere[33]. The observation that the distinctive bleb that grew away from chromite (bleb 7; Fig. S5) is also the least depleted in Fe (Table 1) and the largest in size (i.e., the one having the smallest surface-to-volume ratio, and therefore, the lowest predisposition for massive Fe loss) lends support to this hypothesis. The diffusion of Fe occurred over a period of several days during the slow and gradual cooling of the melt[37] at depth, at a rate of less than 2 °C/h[10]. In contrast to Fe, Ni did not diffuse out of the blebs due to its strong siderophile character and its comparatively low chemical affinity among the crystallizing phases. Given that Fe diffusion in metals is predominantly a vacancy mechanism and that Fe loss was not compensated by a corresponding intake of Ni, vacancies progressively accumulated in the core of some of the blebs, leading to the formation of one or more large cavities (Figs. 2 and S4).

The eruption of basaltic lava onto the lunar surface was accompanied by a more rapid cooling rate of 20–60 °C/h[10]. Initially consisting of large fcc single crystals, the Fe-Ni metal blebs started to transform into small bcc grains when crossing the fcc-to-bcc transformation curve (Fig. 5). The transformation started in the Ni-poor core centers at a temperature of ~550 °C and proceeded radially outwards with further cooling. The rejection of Ni during the fcc-to-bcc transformation is evidenced by its depletion in the crystallizing bcc grains, and its subsequent enrichment in the retained interstitial fcc ones, as well as beyond the core-rim (today's core-intermediate band) interface (Fig. 4). Despite the relatively low temperatures, short-range, nm-scale, Ni diffusion was enabled by the high density of subgrain boundaries and defects in the bcc grains. These features served as fast diffusion pathways, consistent with the observation that Ni diffusion coefficients are several orders of magnitude higher[38–41] in defect-rich Fe-Ni alloys than in the bulk[42]. In other words, Ni atoms did not accumulate at the bcc grain boundaries, as they were continuously removed and stored in the interstitial fcc grains of the core and beyond the core-rim interface. This process may have been facilitated by the volumetric changes associated with the fcc-to-bcc transformation, which, at least temporarily, exerted pressure on the bcc grain boundaries.

The Ni-rich outermost portions of the blebs did not undergo any fcc-to-bcc transformation, as they never crossed M_F throughout the entirety of the cooling process (Fig. 5). Instead, they were stabilized as single-crystal fcc rims, thereby preserving the crystallographic orientation of the parent blebs. One exception is bleb 7, which underwent complete transformation into fcc upon igneous cooling due to its anomalous Ni-poor periphery (see Table 1 and Fig. S5).

Two-stage day- and nighttime surface cooling of lava

The timing of surface igneous cooling could be refined in a serendipitous way based on the microstructures and the chemical compositions observed in the Fe-Ni metal blebs. For the normalized Ni concentration of 19.9 wt% and 23.5 wt% measured on each side of (what was still at that time) the core-rim interface (Table S1), M_F yields a cooling temperature ranging between 90 °C and 160 °C, which is in excellent agreement with the present daytime equatorial to near-equatorial surface temperature of 120 °C reported from direct orbital measurements and computer modeling[43]. This range also aligns with the conditions that prevailed 2.8 Ga ago, when the amount of thermal energy emitted by the Sun was 20% lower but equally counterbalanced by a higher dose of infrared irradiation generated by the hotter Moon's interior. With the sudden temperature drop at lunar dusk, the fcc-to-bcc transformation resumed, pushing the reaction front further outwards. The normalized Ni concentration of 29.7 wt% (Table S1) measured at the interface between the (today's) intermediate band and the rim indicates a temperature of ~160 °C at M_F. This value is ~20 °C higher than the present

https://doi.org/10.1038/s41467-025-57652-6

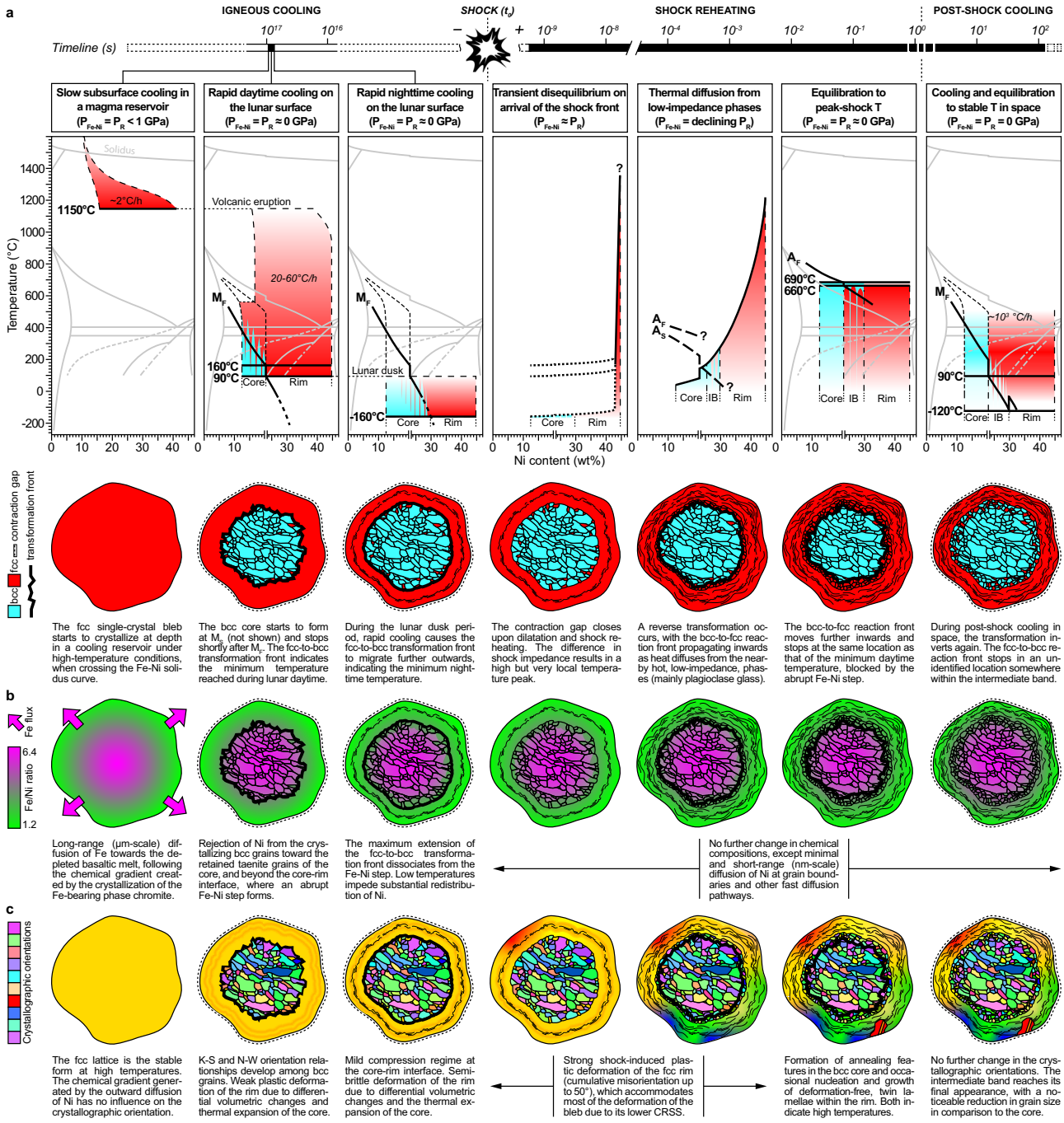

Fig. 5 | Solid Fe-Ni metal blebs as geothermometers. a T-$X_{Fe,Ni}$ binary phase diagrams (top) and artworks (bottom) illustrating the stages of fcc-to-bcc (martensitic) and bcc-to-fcc (austenitic) transformations in a solid Fe-Ni metal bleb, resulting in the nutshell-like microstructure displayed in Fig. 1. The Fe and Ni concentrations have been retrieved from profiles AA′ and CC′ (Fig. 4) and normalized to 100 wt% (Table S1). M_F and A_F have been sourced from existing experimental data[34] (all converted to wt%), and their position and shape have been refined with respect to the presence of alloying elements[93], particle, and grain sizes[68,113–117], and local compression[71,118] (see Supplementary Section 4). The equilibrium phase boundaries[119,120] (light gray) are shown for reference only. Note that the abscissa is discontinuous at the core-intermediate band interface (between 19.9 wt% and 23.5 wt% Ni) to more clearly illustrate the compositional step (seen as double-kinks in M_F and A_F). The low-temperature double-kink in the rightmost T-$X_{Fe,Ni}$ phase diagram reflects the change in grain size between the intermediate band and the rim. For the sake of simplicity and clarity, the squeezing of the bleb shape during shock has not been illustrated in the artwork. **b** Chemical Fe/Ni ratios for the stages shown in (**a**). **c** Crystallographic orientations (in arbitrary colors) for the stages shown in (**a**, **b**).

equatorial to near-equatorial surface temperature reported by the same authors[43], but it is very well in line with the idea of enhanced irradiation from the Moon's interior during the early Eratosthenian period. Hence, our data indicate that the core-rim interface, which shifted from its inner to its outer position at dusk, corresponds to the locations of the daytime and nighttime fcc-to-bcc reaction fronts, respectively. Based on the post-eruption cooling rates of 20–60 °C/h reported in the literature[10], it can be deduced that basalt NWA 479 required 16 to 48 h to reach the daytime surface temperature of 90–160 °C. Furthermore, given the length of lunar days (~350 h), it is probable that this initial surface cooling stage was separated from the second by a rest period during which no fcc-to-bcc transformation occurred.

The two-stage surface cooling process had significant implications for the history of basalt NWA 479. First, it induced the decoupling of the fcc-to-bcc reaction front from the abrupt compositional step (Fig. 4), which was formed by Ni rejection during daytime cooling. The occurrence of such a marked change in composition is important, as it will constitute a major hindrance for the reverse bcc-to-fcc transformation of the major part of the core during shock reheating (see below). Then, the two-stage cooling process indicates that the post-eruption burial depth for basalt NWA 479 was very shallow since lunar day- and nighttime temperatures are homogenized to ~−30 °C at a depth of only 0.4 to 0.8 m[43,44]. Had the rock been located deeper into the lava flow, no shift of the reaction front would have occurred. This view fits well with the high post-eruption cooling rate of 20–60 °C/h reported for this rock[10], and with the very shallow shielding depth of 42 g/cm^2 (equivalent to ~0.1 m considering a density of 3.3 g/cm^3 for mare basalts) deduced from isotopic analyses of stable cosmogenic noble gases[16]. Furthermore, this interpretation is not in conflict with the complex multi-stage cosmic-ray exposure history retrieved from cosmogenic radionuclide concentrations[14,15,17,45]. It is noteworthy, however, that the remarkable freshness of basalt NWA 479 suggests that the rock was likely shielded shortly after crystallization, within the first 10 Ma or so. This could have been achieved by the emplacement of very thin younger lava flows, or overturned regolith layers resulting from the reworking of the uppermost stratigraphic units of the lunar surface[46].

During igneous cooling, the Fe-Ni metal blebs were only mildly affected by deformation. Weak plastic, then semi-brittle, deformation occurred in the rim, first as a consequence of differential contraction[47] of its medial portion (which has an Invar composition) with respect to its inner and outer portions (with ~29.7 wt% and ~44.8 wt% Ni, respectively; see Table S1), and then because of the ~4% volumetric increase accompanying the formation of the bcc core. It is still unclear whether the formation of the intermediate band was influenced by the presence of a compression zone between the growing bcc core and the fcc rim. Nevertheless, we argue that the effect of compression sensu stricto was, at most, marginal. This interpretation is first supported by the presence of a contraction gap between the blebs and the surrounding basalt, which provides some flexibility to accommodate volumetric changes and release pressure. More importantly, intermediate bands have also been observed in hollow blebs (see bleb 4 in Fig. S4), in which the large internal cavity can readily accommodate the volumetric change resulting from the fcc-to-bcc transformation of comparatively small core fragments. This observation is incompatible with the hypothesis that the intermediate bands are formed by compression. Therefore, at the end of igneous cooling, the Fe-Ni metal blebs consisted of a core of small bcc (and retained fcc) grains, a prominent compositional step disrupting the smooth and gradual core-to-rim Fe-Ni zoning, and further outwards, a mildly deformed single-crystal fcc rim. In this regard, the broad outlines of the nutshell-like microstructure were already established at the end of the igneous cooling phase.

Long incubation time inhibiting full bcc-to-fcc reversal upon shock

The tremendous amount of energy released by the impactor during the shock pulse had a very significant influence on the microstructures of the Fe-Ni metal blebs. The features attributed to shock metamorphism include the closure of the contraction gaps, the strong plastic deformation of the fcc rims, the thermal annealing of bcc grains in the core centers, and the sporadic recrystallization of the fcc rims into deformation-free twin lamellae. The initial response to shock, however, differed significantly between the hollow and the solid Fe-Ni metal blebs (see Supplementary Section 2). In the former, the large internal cavities collapsed entirely upon shock, inducing local melting and quenching into Fe-Ni-rich glass, and the complete reversal of the bcc cores into fcc. In contrast, the cores of the solid blebs did not transform back into fcc (except in their outermost portions, where they formed the intermediate bands; see below). The complete reset of the microstructures in the hollow blebs made it clear that they were no longer suitable for use as thermal indicators. We therefore focused our attention exclusively on the solid ones.

At the onset of shock, the closure of the contraction gaps surrounding the solid Fe-Ni metal blebs locally absorbed part of the shock energy, thereby compensating for the transient high-pressure spikes occurring in the first tens of nanoseconds after impact. However, this process was much too ephemeral to withstand the high-pressure conditions that persisted throughout the shock pulse. It is well established that athermal transformations (both forward and reverse) occur almost instantaneously once initiated, at a velocity ranging between one-fourth and the speed of sound in matter. Given the velocity at which this process occurs in Fe-Ni alloys (i.e., between ~0.25 and ~3.0×10^3 m/s)[48–51], it was to be expected that the cores would undergo a reverse transformation into hexagonal close packing (hereafter hcp) during the time interval spent at high pressure. However, this view is not supported by TEM analyses. In particular, the cores of the solid blebs do not display the high-pressure indicators typically observed in similar structures (Fig. 1). The absence of features such as remnants of mechanical twins of specific variants at the intersection between habit planes[52], a dense network of straight dislocations in glide configuration coupled with the presence of stacking faults[53], or aligned bcc grains transformed back from hcp laths[54], and a reduced grain size compatible with the hypothesis of back-and-forth transformation-induced grain size reduction[55–57], indicates that a reversal into hcp did not occur. The lack of evidence for a reverse transformation is puzzling, given that the pressure (and/or temperature) conditions experienced by the Fe-Ni metal blebs undoubtedly resulted in a brief excursion outside the bcc stability field during the shock pulse.

This conundrum may be explained by considering the amount of time, referred to as the incubation period, required for the reverse transformation to be initiated, vs the time spent by the rock under pressure. In contrast to pure Fe and most lean-alloyed steels[58], forward and reverse transformations in Fe-Ni alloys may occur isothermally[59,60]. This suggests that, under specific conditions, transformation only starts after the incubation period has elapsed beyond the transition curve. Additionally, isothermal transformation is characterized by a certain degree of sluggishness at the outset of crystal growth, with velocities as low as 10^{-5} m/s[61–63]. This process has been demonstrated convincingly for decades by the shift and flattening of the transformation curves in diagrams plotting time vs transformed fractions, primarily in Mn-bearing Fe-Ni alloys[64–66], but also in Mn-free Fe-Ni metals[67]. Isothermal transformations in Fe-Ni alloys are reinforced by the presence of very low carbon concentrations[61,62], small particle or grain sizes (with incubation periods up to ~10^4 s for diameters smaller than 5 µm)[68], and hydrostatic pressure (with incubation periods up to ~10^3 s for samples pressurized below 1 GPa)[69,70]. It should be noted that this latter argument is controversial, as hydrostatic pressure and shock loading (which is of particular importance in the context of meteorite impact) generally show the exact opposite effect on incubation times. In essence, while hydrostatic pressure increases the incubation time, shock loading tends to reduce it[71–76]. The sole shock-loading experiment conducted to quantify the incubation period in the bcc-to-fcc reversal of Fe-Ni alloys corroborates this statement[77], with nucleation starting after only ~10^{-7} s. However, these results were obtained from comparatively coarse-grained Fe-Ni alloys. In light of the major influence of grain size on the duration of incubation periods in Fe-Ni alloys[68], and, to a lesser extent, the low carbon content derived from the strongly reduced parent magma, we favor the hypothesis of delayed and sluggish nucleation and reverse transformation hindered by the occurrence of a protracted incubation period.

In order to substantiate this hypothesis, it is necessary to weigh the duration of the incubation period against that of the shock, which is defined here as the time spent by the rock at high pressure. The fundamental premise is that, if the incubation period exceeded the duration of the shock pulse, no reverse transformation of the cores could have occurred. Recent numerical simulations have shown that, for a given impact, the shock duration is primarily influenced by the burial depth (especially in shallow rocks[78]), and, to a lesser extent, the shock pressure and the impactor size. The role of the impactor velocity is increasingly regarded as inconsequential or secondary[79]. The available data indicate that the burial depth of basalt NWA 479 never exceeded a few meters[16,17,45], which is consistent with the long-standing observation that all the lunar meteorites studied to date were excavated from surprisingly shallow grounds[80]. It is, however, indisputable that the rock experienced a complex, and as yet unclear, multi-stage cosmic-ray exposure history. The residual concentrations of cosmogenic radionuclides[17,45] indicate a burial depth of ~1100 g/cm^2, which has been interpreted as the ejection depth by the same authors. When converted into metric units, this corresponds to ~6.1 m (assuming that the overlying material is solely made of compacted regolith; ρ = ~1.8 g/cm^3), ~4.3 m (with equal proportions of regolith and basaltic lava; ρ = ~2.6 g/cm^3), or ~3.3 m (with basalt only; ρ = ~3.3 g/cm^3). In contrast to the first value, the second is more closely aligned with the commonly reported maximum ejection depth of ~4.0 m for lunar meteorites[81]. The third value is contingent upon the improbable scenario in which the regolith would be entirely absent. An additional possibility is that the meteorite was ejected from the uppermost layer of uncompacted regolith at a depth of ~42 g/cm^2, i.e., ~0.3 m (with ρ = ~1.5 g/cm^3)[82], as suggested from noble gas stable isotopic analyses[16]. Therefore, despite the remaining uncertainty regarding the ejection depth, which obscures the ejection process (i.e., jetting[83,84], spallation[85,86], vs standard excavation), the evidence does not invalidate the hypothesis of a shallow origin for basalt NWA 479.

The correlation between ejection depth and shock duration has been recently investigated using hydrocode simulations[79]. Caution is required in their use here, however, as some of the initial assumptions may not be directly applicable to lunar impacts. In essence, while the hydrocode simulations currently available have focused on vertical impacts on Mars-sized planetary bodies having the mechanical strength of basalt[79], a more robust determination of the shock duration in our case would require consideration of several additional factors. These include the stronger ejection efficiency[81] and higher probability[87] of oblique impacts, the poorer mechanical strength of loose regolith compared to competent basalt[82], and the lower lunar escape velocity (2.38 km/s vs 5.03 km/s). The incorporation of these inputs into hydrocode simulations is currently underway, but the results are not yet available. It is currently believed that obliquity moderately increases the shock duration, potentially by a factor of two or three[79], since oblique impacts significantly increase the maximum ejection depth[81]. Loose or weakly cemented materials reduce the maximum ejection depth[88], but the change in shock duration is negligible when shallow grounds are considered (B.C. Johnson, personal communication). Finally, a reduction in the escape velocity exerts a significant influence on shock duration, enabling ejection from depths that are comparatively greater. In consideration of the available evidence[79], it can be posited that the lower lunar escape velocity would result in a slight increase in the shock duration, potentially by a factor of two or less. In conclusion, it can be proposed that the combined effects of obliquity and a lower escape velocity have increased the shock duration, although to a lesser degree than that observed in available hydrocode simulations[79]. Based on realistic impactor radii (5–15 m depending on the conditions[80,81]) compatible with the small size[89] of young lunar craters (ejection of basalts NWA 479 and NWA 032 dates back to ~50 ka[16,17]), and taking into account the specificities of oblique lunar impacts, it can be estimated that the shock duration in basalt NWA 479 lasted between 10^{-4} and 10^{-2} s. This time interval is in good agreement with the "small impact" scenario[80] and the early numerical simulations of impacts and meteorite trajectories. These studies have demonstrated that all the lunar meteorites studied to date were initially slow-moving (2.38–3.00 km/s) ejecta[90] excavated from craters as small as 450 m in diameter[91]. In addition, it should be noted that the aforementioned interval encompasses the pressure decline, which means that the duration at maximum pressure is even shorter, probably in the range of 10^{-4} to 10^{-3} s. Therefore, despite the remaining uncertainties, there is little doubt that basalt NWA 479 was ejected from shallow grounds during a very short shock pulse. The brevity of the shock in comparison to the considerably longer duration of the incubation period (see above) suggests that no reverse transformation, either into hcp, or into fcc, occurred in the core of the solid Fe-Ni metal blebs at this early stage of the shock history.

Deferred peak-shock heating from vesicular plagioclase melt

With a brief shock pulse of only 10^{-4} to 10^{-3} s, the bulk of the solid Fe-Ni metal blebs only began to heat significantly at the end of the pressure decline and continued to do so after release to the near-perfect vacuum of the outer space. As anticipated based on their inherently high shock impedance, the blebs remained at a low temperature for the first tens of nanoseconds after impact. The nearly instantaneous thermal anomaly was extremely local and brief, making it unable to significantly heat the bulk of the blebs (see Supplementary Section 2). Consequently, the transfer of heat towards the blebs only became substantial after a brief delay, initiated by thermal conduction from the hot, vesicular, plagioclase melt. Heat transfer from the other phases of the rock also occurred, albeit at a much lower rate and down a smoother gradient. This is consistent with their weak to moderate shock impedance and inability to act as efficient heat sources.

The exact duration of heat transfer through conduction is uncertain, but it likely persisted at least until the restoration of the contraction gaps. A lower bound can be inferred from the vesiculation of plagioclase, which unambiguously indicates that it was still molten, and, therefore, in close contact with the blebs, after decompression to zero pressure, i.e., ~10^{-3} s after shock at least (see above). This minimum value is supported by heat transfer simulations using the Energy2D software[92], which show that plagioclase reached the melt-glass transition temperature, ~1450° at 0 GPa, in <~10^{-2} s. As the temperature decreased further, the mode of heat transfer shifted from conduction to radiation. This transition was initiated by the reopening and widening of the contraction gaps between the blebs and the surrounding phases (except in the rare locations where the blebs were still in contact with the nearby phases). The change in the mode of heat transfer and the drastic reduction in contact areas resulted in a less effective and heterogeneous heat flux. It can thus be concluded that most of the heat was transferred to the blebs by conduction from the hot plagioclase melt within the first ~10^{-2} s after shock.

In this interpretation, the intermediate band is the result of a reverse transformation of the core outer border from fcc to bcc. The interface between the core and the intermediate band, initially delineated during daytime igneous cooling, represents the maximum inwards extension of the bcc-to-fcc reaction front. The occurrence of daytime igneous cooling and shock reheating reaction fronts at the very same location is not fortuitous, as this corresponds to the abrupt compositional step that formed early in the magmatic history of the blebs. During shock reheating, this step acted as a barrier to the further inward bcc-to-fcc reverse transformation of the cores. By integrating the effects of alloying elements[93] and grain size[94] in the T-$X_{Fe,Ni}$ binary phase diagram, temperatures of 660 °C at 23.0 wt% Ni and 690 °C at 17.2 wt% Ni (Fig. 5) were obtained (see also Supplementary Section 4.4). This interval, corresponding to the location of the bcc-to-fcc reaction front at the core-intermediate band interface, is interpreted as the

equilibrium peak-shock temperature reached shortly after shock by thermal diffusion.

Shock reheating followed by rapid post-shock cooling

The time required to achieve full peak-shock thermal equilibrium throughout the rock (including the thick shock melt veins, the plagioclase glass, the rock-forming silicates, and the Fe-Ni metal blebs) was substantial, as it followed a logarithmic equilibration path. The calculations based on the Stefan problem[95] indicate that the duration was at least 1 s (see Supplementary Section 5). It is also noteworthy that the heating curve of the blebs is likely to have varied slightly from one location to another. These discrepancies can be attributed to several factors, including local differences in modal composition, the heterogeneous distribution and size of additional heat sources (shock melt veinlets, veins or pockets), the occurrence of thermal conduction barriers (cracks, interphase boundaries, planar defects), the processes consuming or releasing heat (plastic deformation, phase transitions, etc.), and the insulation effect induced by the large phenocrysts having moderate shock impedances.

In addition, it must be remembered that meteorite NWA 049 was ejected from the lunar surface as a very small rock[12], ~2.9 to ~7.0×10^{-2} m in radius depending on the type of pairing with meteorite NWA 032, and the percentage of mass lost through ablation upon atmospheric entry[81]. Using numerical simulations[96] and assuming the smallest meteorite size (i.e., the most dynamic scenario), it can be calculated that meteorite NWA 049 may have cooled down from its equilibrium peak-shock temperature (660–690 °C) to its post-shock residence temperature in space in a few seconds only (see below and Supplementary Section 5). This time-lapse was certainly shorter near the meteorite surface, where the cooling rate was higher. In light of the extended period of shock reheating and the sudden post-shock cooling, it cannot be definitively asserted that the blebs located at the periphery of the meteorite or trapped within large insulating phenocrysts have even reached complete peak-shock thermal equilibrium.

Unequivocal evidence for which the shock reheating curve would have been superseded by post-shock cooling has not been found. There are two main reasons for this. Firstly, the former meteorite outer envelope was ablated on atmospheric entry, thus escaping analysis forever. Secondly, no Fe-Ni metal bleb trapped in the center of a large phenocryst has been observed in the subsample studied here. Nevertheless, the features observed in blebs 3 (Fig. S3) and 7 (Fig. S5) lend some credibility to this hypothesis. Bleb 3 is the only bleb fully encapsulated within a phenocryst, thereby isolated from the groundmass. Given the unusually high Ni concentration measured in its center (Table 1), it should display a fully back-transformed, sub-microgranular, intermediate band-like core. This is, however, not the case here. One possible explanation is that the equilibrium peak-shock temperature was not reached in this bleb due to the insulating effect provided by the phenocryst. An alternative hypothesis is that the feature is an artifact resulting from peripheral sectioning of the bleb, with the X-ray emission volume of WDS analyses sampling both the core and the underlying rim (plus shallow retained fcc grains). This geometry would result in an erroneous increase in the Ni content, making it incoherent with the observed microstructures. In view of the unusual thickness of the fcc rim and the peripheral entrapment of this bleb within the olivine phenocryst (thereby minimizing any potential insulating effect), we conclude that the observed feature is an artifact, and that there is no compelling evidence for unachieved thermal equilibrium. Nevertheless, the residual uncertainty that full equilibrium may not have been reached everywhere in the rock indicates that the widely accepted term "equilibrium peak-shock temperature" used throughout the paper may actually reflect a "near-equilibrium" situation. In light of the thermal equilibration time estimated by others[97] and considering the logarithmic behavior of thermal diffusion processes, however, it can be stated with confidence that meteorite NWA 049 was, in the worst case, very close to thermal equilibrium when post-shock cooling started.

Bleb 7 is intriguing in many ways (Fig. S5). In contrast to the other blebs, it is not rimmed by an fcc single crystal, but rather by a composite fcc-bcc rim that is structurally similar to the intermediate bands described earlier. The smooth Fe-Ni zoning and the anomalously high peripheral Fe content (Table 1) convincingly account for this peculiarity. In addition, the composite fcc-bcc rim is the thickest when in contact with plagioclase glass, and the thinnest when separated from the moderate shock-impedance minerals (pyroxene phenocrysts) by a contraction gap. The uneven advance of the bcc-to-fcc transformation front upon shock provides evidence that thermal diffusion occurred preferentially from the hot plagioclase melt and markedly slowed down with the restoration of the contraction gap. This may also indicate that the final heating of the bleb was abruptly interrupted by post-shock cooling of the meteorite in space. In this interpretation, bleb 7 can be regarded as an illustrative example of thermal "near-equilibrium", indicating that shock reheating did not fully reach completion. However, the distance between the location of bleb 7 and the primitive (pre-ablation) meteorite surface is unknown, thus rendering any conclusive statement purely conjectural. Besides this, bleb 7 displays additional characteristics that suggest a complex shock history. The small size of the bcc grains in the core and the spread of Kurdjumov-Sachs[25] and Nishiyama-Wassermann[26,27] inter-grain orientation relationships are usually observed in hollow Fe-Ni metal blebs that have undergone a complete back transformation during shock. The presence of these characteristics in bleb 7 suggests that it also underwent back-and-forth recrystallization, however not because of pore collapse, but possibly because of its unusual location within the rock. Bleb 7 is caught between two pyroxene phenocrysts and along the trajectory of thin shock melt veins (Fig. S2). In comparison to the other solid blebs, it was subject to a significantly greater degree of shear, with limited space to accommodate it. We therefore propose that bleb 7 underwent a complete back-and-forth transformation at the onset of shock as a consequence of lattice strain induced by intense shearing, rather than as a result of pore collapse. This assumption is supported by the ARPGE reconstructions, which indicate the presence of deformation twinning (see the [111] fcc pole figures and the parent orientation map in Fig. S5). Added to this, the parent grain distribution suggests that the bleb has an upper and lower portion, with a boundary roughly parallel to the borders of the adjacent phenocrysts and on the trajectory of the shock melt veins. At the end of the shock stage, the small, freshly reset, bcc grains that constituted the entirety of bleb 7 were subjected to the same heat flux from the neighboring vesiculated plagioclase glass, which resulted in the formation of the composite fcc-bcc rim still visible today.

To sum up, while the observed features in blebs 3 and 7 have not the value of evidence for incomplete thermal equilibrium, they clearly suggest that the Fe-Ni metals trapped in large phenocrysts or located at the periphery of the meteorite may not be suitable for geothermometry.

The post-shock residence temperature reached after ejection into space can also be inferred from Fig. 5, albeit with less accuracy than the values obtained for the other thermal stages of the rock history. This is because the fcc-to-bcc transformation front corresponding to the post-shock thermal equilibrium could not be identified with certainty within the intermediate band. With grains often smaller than the thickness of the TEM foil itself, the method clearly reached its limits here. In the absence of a clear reaction front corresponding to this stage, the best possible temperature range that can be deduced from Fig. 5 corresponds to the intersection of M_F with the inner and outer interfaces of the intermediate band, namely at −120 °C and 90 °C, respectively. This interval is robust despite its wide span, as it encompasses the much narrower range (0–50 °C) obtained from the well-established calculation method based on solar absorptance and hemispherical emittance[98] (see Supplementary Section 5).

High peak-shock temperature and the small impact scenario

To recapitulate, the combination of sub-microstructural features with geochemical data derived from the Fe-Ni metal blebs, coupled with the use of refined T-$X_{Fe,Ni}$ phase diagrams, allowed us to explain the thermal history of lunar basalt/meteorite NWA 049 in great detail (Fig. 5). Our findings indicate that the cooling of the lava occurred in two stages: first down to 90–160 °C during lunar daytime, and then down to −160 °C during lunar nighttime. Following the collision with a moderate-velocity impactor, the equilibrium peak-shock temperature of 660–690 °C was reached after pressure release via conduction from hot vesicular plagioclase. Post-shock cooling in outer space did not last more than seconds or minutes, depending on the ejection size of the meteorite. The residence temperature in space was between −120 °C and 90 °C (refined to 0 °C and 50 °C from calculations by other means).

The peak-shock temperature of 660–690 °C reported here is well above the value of 200 °C reported in a recent review of the paired meteorite NWA 032[99]. One explanation could be that meteorites NWA 479 and NWA 032 are launch pairs, ejected from the lunar surface upon the same impact but as separate rocks, rather than fall pairs, broken apart on atmospheric entry. However, the occurrence of vesicles was not identified in the aforementioned study[99], whereas they are pervasively present in meteorite NWA 049 and in at least one subsample of meteorite NWA 032 (see Fig. S6c). Given the pivotal role of vesicular plagioclase in estimating peak-shock conditions, we hypothesize that the misidentification of the nature of plagioclase glass may have prompted the authors to underestimate the equilibrium peak-shock temperature[99].

In any case, the results presented here are in excellent agreement with the microstructures observed in our subsample of meteorite NWA 479, both inside and outside the Fe-Ni metal blebs. The presence of plastically deformed fcc rims, occasional recrystallization of the rim into deformation-free fcc twin lamellae, and annealing of bcc grains within the cores provide evidence that the equilibrium peak-shock temperature was several hundreds of degrees Celsius. In addition, the pervasive occurrence of vesicles and Si-rich blobs in plagioclase glass, which constitutes 20–30 vol% of the groundmass[10], indicates that a significant portion of the rock was still above ~1450 °C immediately after pressure release. Moreover, the abundance of shock melt veins, with the thickest measuring over 1 mm (Fig. S1), is indicative of sustained heating, albeit on a more localized scale. In conjunction with the presence of strong mosaicism and planar deformation features in olivine, the arguments above collectively point to intense shock heating.

In conclusion, our results suggest that high peak-shock temperatures can be reached in meteorites excavated during brief impacts (~10^{-3} s), from very shallow grounds (a few meters at most) and small craters (up to a few hundred meters in diameter). This finding challenges the long-held assumption that equilibrium peak-shock temperatures are necessarily associated with strong events, high impactor velocities, and shock energies. According to the most up-to-date shock classification scales[78,100], the microstructural features observed in meteorite NWA 479 point to a “strong” shock. This diagnostic, unquestionable from a microstructural point of view, modifies our perspective on the “small impact” scenario put forward over the years[80] for recent lunar impacts, including the one that excavated meteorite NWA 479. It is beyond the scope of this study to determine whether this apparent contradiction will be resolved by ongoing and future hydrocode simulations. There is no doubt, however, that incorporating variables such as impact obliquity onto grounds similar to the lunar surface will enhance our comprehension of shock-induced thermal processes, including those observed for meteorites excavated by jetting or spallation. Thus, our results stress that extreme caution is required when correlating impactor size and velocity, burial depth, crater size, and peak-shock pressures and temperatures, with the observed microstructures. This is particularly relevant for meteorites containing vesicular plagioclase glass, for which, by the own admission of one of its strongest advocates[101], the occurrence of high-pressure mineral assemblages is unreliable.

The data presented here indicate that iron-rich metals offer valuable advantages over standard geothermometers for tracking the full thermal history of extraterrestrial rocks. The distinction between diurnal and nocturnal cooling on the lunar surface, the disentangling of the very short-lived processes occurring during shock reheating, and, to a lesser extent, post-shock cooling have demonstrated that Fe-Ni alloys are highly effective geothermometers applicable to a very wide range of temperatures and timescales. It is, therefore, to be expected that the microstructures of native metals occurring in terrestrial rocks, such as in (rare) basalts, peridotites, kimberlites, or metallogenic hydrothermal deposits, will gain in popularity in the next few years. Finally, our study emphasizes the importance of standardizing the use of sub-microstructural techniques often overlooked in planetary sciences, such as EBSD or ACOM, as they offer a promising avenue for resolving contentious issues.

Methods

SEM imaging

A subsample of lunar meteorite NWA 479 was hot pressed in conductive resin using a Struers CitoPress-1 apparatus. The sample surface was stepwise diamond-polished down to a grade of 0.5 µm and coated with a 15-nm carbon layer to prevent charging under the electron beam.

Backscatter electron (BSE) images were obtained at the Institute of Earth Sciences at the University of Lausanne (UNIL) using a Tescan Mira II LMU FE-SEM operated at an acceleration voltage of 20 kV and a probe current of ~0.4 nA. The nutshell-like microstructures of the Fe-Ni metal blebs were imaged in high-contrast BSE mode using a probe current value of ~15 nA and a very long dwell time to maximize the signal-to-noise ratio.

EBSD crystallographic orientation mapping

As EBSD requires a surface of analysis that is free of mechanical damage, the SEM mount was polished in an alkaline (pH = 9.8) aqueous suspension of colloidal silica. No carbon coating was applied in order to ensure optimal pattern quality. EBSD analyses were carried out in the Tescan Mira II LMU FE-SEM operated at an acceleration voltage of 20 kV, a probe current of ~1.1 nA, and a dwell time of 0.15 s. The sample surface was tilted at 70° with respect to the horizontal and placed at a working distance of 23 mm. The EBSD patterns were acquired using a Nordlys S camera and the AZtec software package from Oxford Instruments. The Fe-Ni metals were indexed using a refined version of the structure files of fcc- (a = 3.58 Å) and bcc- (a = 2.86 Å) iron, which were generated with the Twist software included in the Channel 5 software package. The raw data consisted of orientation matrices, 300 × 400 pixels in size, collected at step sizes ranging between 25 and 50 nm.

Post-processing started with the removal of the poorly indexed data points, i.e., those exhibiting a mean angular deviation >1.3° or a band contrast <20). The matrices were noise-reduced in accordance with the established wildspike correction methodology and a six-neighbor zero solution extrapolation. The processed data were represented as pole figures of Euler angle triplets (φ_1, Φ, φ_2), and the maps were color-coded according to the phase, inverse pole figure, or cumulative misorientation schemes. The black lines on the maps delimit misorientations exceeding 1° between neighboring pixels, thereby emphasizing the presence of subgrain and grain boundaries. For further details regarding the determination of parent grain orientations using the ARPGE software, please refer to the relevant literature[24].

EPMA-WDS chemical analyses

The chemical compositions of the trace, minor, and major elements in the Fe-Ni metal blebs were determined at UNIL through wavelength

dispersive spectrometry (WDS). The WDS system was attached to a JEOL JXA-8530F HyperProbe electron probe microanalyzer (EPMA), operated at an acceleration voltage of 15 kV and a probe current of 15 nA. X-ray intensities and peak-to-background ratios were measured from Kα and Lα lines using a combination of standard and large LIF, PET, TAP, and LDE crystals to enhance sensitivity and counting statistics.

FIB preparation of the TEM foil

The preparation of a site-specific, electron-transparent, thin foil was a prerequisite for the planned analyses in the transmission electron microscopes (TEM). The selection of Fe-Ni metal bleb 1 (Figs. 1, 4, and S3) was based on two criteria. Firstly, the absence of a central cavity made it suitable for use as a geothermometer (for further details, please refer to the main text and Supplementary Sections 2.2 and 2.3). Secondly, the nearby phase association was deemed to be representative of the majority of the Fe-Ni metal blebs in meteorite NWA 479, particularly in terms of proximity to chromite.

The clearance of the foil from the bulk sample and its thinning to electron transparency was conducted in a Zeiss nVision 40 dual beam focused ion beam (FIB) FE-SEM at the Interdisciplinary Center for Electron Microscopy (CIME) of the Ecole Polytechnique Fédérale de Lausanne (EPFL) using the sputtering action of heavy gallium ions accelerated at a voltage of 30 kV. Prior to the milling process, the area of interest was coated in situ with a protective, 3 µm-thick, carbon layer obtained from the dissociation of organic molecules injected in gaseous form into the FIB-FE-SEM chamber. The abrasion rate of the sample was monitored by adjusting the ion probe current intensity, first stepwise down from 45 nA to 1.5 nA to facilitate the clearance of the foil, and then down to 80 pA during the thinning step to limit amorphization of the foil surface. During the fine milling procedure, the Gaussian profile of the ion beam was compensated by tilting the specimen at an angle of 1.5° to 2.0° with respect to the incident ion beam. Because of the markedly disparate abrasion resistance of the carbon protective layer, the Fe-Ni metal bleb, and the surrounding silicate minerals, the specimen tilt was meticulously and consistently adjusted throughout the process. The final step in the preparation of the foil entails cleaning under smooth ion beam conditions (2 kV and 25 pA) at a tilt angle of 3°. The TEM-ready foil, approximately 15 × 10 × 0.1 µm in size, was transferred onto a FIB lift-out grid using Kleindiek micromanipulators. For a comprehensive account of the FIB technique, please refer to other sources[102–106].

TEM imaging and EDS chemical analyses

Bright-field (BF), dark-field (DF), and high-angle annular dark-field (HAADF) images were obtained at EPFL from the FIB thin foil using an FEI Tecnai Osiris FE-TEM equipped with an ultra-high brightness source. The instrument was operated at an acceleration voltage of 200 kV. The TEM diffraction patterns were collected on a Gatan Orius CCD digital camera and indexed offline using the JEMS electron microscopy simulation software[107].

The concentrations of Fe, Ni, and Co were determined using the same instrument in scanning TEM (STEM) mode at a spatial resolution of 1–2 nm. A twin-pole piece with a Super-X EDS module containing four silicon drift detectors was used to ensure high-speed and high-sensitivity measurements. The raw EDS data were then post-processed offline using the Bruker Esprit 1.9 software package in order to obtain quantified chemical abundances.

ACOM crystallographic orientation analyses

Ultra-high spatial resolution ACOM was performed at EPFL using a JEOL JEM 2200FS FE-TEM equipped with the NanoMegas ASTAR system[108]. The instrument was operated in nano-beam diffraction (NBD) mode, with the objective of reducing the size of the electron probe to a minimum. The acquisition parameters included an acceleration voltage of 200 kV, a C2 condenser lens aperture of 10 µm, an excitation of the condenser minilens corresponding to an alpha value of 3, and a camera length of ~180 mm. These settings yielded a highly focused electron probe with a diameter of 2 nm and a convergence semi-angle of 0.8 mrad. Orientation maps comprising 800 × 800 pixels were collected at a step size of 2 nm and a dwell time of ~0.01 s, resulting in acquisition times of <2 h per map. For each point of the scan, a diffraction pattern was displayed on a fluorescent screen, captured by a digital CCD camera, and stored for offline indexing. In contrast to the indexing routine of EBSD patterns, which requires the prior identification of Kikuchi band triplets, the procedure used in ACOM is based on template matching, that is the assessment of the goodness-of-fit between the measured and the simulated diffraction patterns. The ASTAR software package was used to generate a template library comprising simulated diffraction patterns for all possible crystallographic orientations. The input data for fcc and bcc iron were the existing CIF files with unit cell dimensions of 3.58 Å and 2.86 Å, respectively.

The raw orientation data were imported into MTEX, an open-source MATLAB toolbox designed for data treatment and texture analysis[109]. The procedure followed was very similar to that described in full detail elsewhere[110,111]. In brief, post-processing consisted of a rotation of the dataset to align the ASTAR and MTEX orientation frames. A filtering routine was executed to reduce noise, and another one to correct for the typical 180° ambiguity frequently encountered in ASTAR. Finally, the data were exported as ANG files and imported into the Channel 5 software suite, in which a noise-reduction routine similar to that applied to EBSD data was implemented.

Data availability

The subsample of meteorite NWA 479 containing the Fe-Ni metal blebs investigated here is the property of P.G. The crystallographic and chemical data, including EBSD, ACOM, TEM-EDS maps, and profiles, along with WDS analyses, are available at the following address: https://doi.org/10.6084/m9.figshare.27926835.

References

1. Meibom, A. et al. Large-scale thermal events in the solar nebula: Evidence from Fe,Ni metal grains in primitive meteorites. *Science* **288**, 839–841 (2000).
2. Stöffler, D., Keil, K. & Scott, E. R. D. Shock metamorphism of ordinary chondrites. *Geochim. Cosmochim. Acta* **55**, 3845–3867 (1991).
3. Smith, B. A. & Goldstein, J. I. The metallic microstructures and thermal histories of severely reheated chondrites. *Geochim. Cosmochim. Acta* **41**, 1061–1072 (1977).
4. Goldstein, J. I., Scott, E. R. D. & Chabot, N. L. Iron meteorites: crystallization, thermal history, parent bodies, and origin. *Geochemistry* **69**, 293–325 (2009).
5. Yang, J., Goldstein, J. I. & Scott, E. R. D. Iron meteorite evidence for early formation and catastrophic disruption of protoplanets. *Nature* **446**, 888–891 (2007).
6. Scott, E. R. D., Krot, T. V., Goldstein, J. I. & Wakita, S. Thermal and impact history of the H chondrite parent asteroid during metamorphism: constraints from metallic Fe-Ni. *Geochim. Cosmochim. Acta* **136**, 13–37 (2014).
7. Lindsley, D. H. Pyroxene thermometry. *Am. Miner.* **68**, 477–493 (1983).
8. Clayton, R. N. Oxygen isotopes in meteorites. *Ann. Rev. Earth Planet. Sci.* **21**, 115–149 (1993).
9. Nakamuta, Y. & Motomura, Y. Sodic plagioclase thermometry of type 6 ordinary chondrites: implications for the thermal histories of parent bodies. *Met. Planet. Sci.* **34**, 763–772 (1999).
10. Fagan, T. J. et al. Northwest Africa 032: product of lunar volcanism. *Met. Planet. Sci.* **37**, 371–394 (2002).

11. Barrat, J. A. et al. Lithium behaviour during cooling of a dry basalt: an ion-microprobe study of the lunar meteorite Northwest Africa 479 (NWA 479). *Geochim. Cosmochim. Acta* **69**, 5597–5609 (2005).
12. Barrat, J. A. et al. News from the moon and mars: preliminary examinations of two Saharan finds. *Proc. Lunar Planet. Sci. Conf.* **32**, 1317 (2001).
13. Borg, L. E. et al. Mechanisms for incompatible-element enrichment on the Moon deduced from the lunar basaltic meteorite Northwest Africa 032. *Geochim. Cosmochim. Acta* **73**, 3963–3980 (2009).
14. Fernandes, V. A., Burgess, R. & Morris, A. ^{40}Ar-^{39}Ar age determinations of lunar basalt meteorites Asuka 881757, Yamato 793169, Miller Range 05035, La Paz Icefield 02205, Northwest Africa 479, and basaltic breccia Elephant Moraine 96008. *Met. Planet. Sci.* **44**, 805–821 (2009).
15. Fernandes, V. A., Burgess, R. & Turner, G. ^{40}Ar-^{39}Ar chronology of lunar meteorites Northwest Africa 032 and 773. *Met. Planet. Sci.* **38**, 555–564 (2003).
16. Lorenzetti, S., Busemann, H. & Eugster, O. Regolith history of lunar meteorites. *Met. Planet. Sci.* **40**, 315–327 (2005).
17. Nishiizumi, K. & Caffee, M. W. Exposure histories of lunar meteorites Northwest Africa 032 and Dhofar 081. *Proc. Lunar Planet. Sci. Conf.* **32**, 2101 (2001).
18. Goldstein, J. I. & Axon, H. J. Composition, structure, and thermal history of metallic particles from 3 Apollo 16 soils, 65701, 68501, and 63501. *Proc. Lunar Sci. Conf.* **4**, 751–775 (1973).
19. Goldstein, J. I. & Blau, P. J. Chemistry and thermal history of metal particles in Luna 20 soils. *Geochim. Cosmochim. Acta* **37**, 847–855 (1973).
20. Askeland, D. & Wright, W. J. The science and engineering of materials (Cengage Learning, Boston, 2016).
21. Mlikota, M. & Schmauder, S. On the critical resolved shear stress and its importance in the fatigue performance of steels and other metals with different crystallographic structures. *Metals* **8**, 883 (2018).
22. Guo, E. N. et al. Mechanical characterization of microstructures in a cast duplex stainless steel by micropillar compression. *Mater. Sci. Eng. A* **598**, 98–105 (2014).
23. Cheng, G. M. et al. Grain size effect on deformation mechanisms of nanocrystalline bcc metals. *Mater. Res. Lett.* **1**, 26–31 (2013).
24. Cayron, C. ARPGE: A computer program to automatically reconstruct the parent grains from electron backscatter diffraction data. *J. Appl. Crystallogr.* **40**, 1183–1188 (2007).
25. Kurdjumov, G. V. & Sachs, G. Über den mechanismus der Stahlhärtung. *Z. Phys.* **64**, 325–343 (1930).
26. Wassermann, G. Einfluß der α-γ-Umwandlung eines irreversiblen Nickelstahls auf Kristallorientierung und Zugfestigkeit. *Arch. Eisenhüttenwes.* **6**, 347–351 (1933).
27. Nishiyama, Z. X-ray investigation of the mechanism of the transformation from face centered cubic lattice to body centered cubic. *Sci. Rep. Tohoku* **23**, 637–644 (1934).
28. Smigelskas, A. D. & Kirkendall, E. O. Zinc diffusion in alpha brass. *Trans. AIME* **171**, 130–142 (1947).
29. Bhadeshia, H. K. D. H. Bainite in steels - theory and practice (Maney Publishing, Leeds, 2015).
30. Hartlieb, P., Toifl, M., Kuchar, F., Meisels, R. & Antretter, T. Thermo-physical properties of selected hard rocks and their relation to microwave-assisted comminution. *Miner. Eng.* **91**, 34–41 (2016).
31. Tanji, Y. Thermal expansion coefficient and spontaneous volume magnetostriction of Fe-Ni (fcc) alloys. *J. Phys. Soc. Jpn.* **31**, 1366–1373 (1975).
32. Weitz, C. M., Rutherford, M. J. & Head, J. W. Oxidation states and ascent history of the Apollo 17 volcanic beads as inferred from metal-glass equilibria. *Geochim. Cosmochim. Acta* **61**, 2765–2775 (1997).
33. Weitz, C. M., Rutherford, M. J., Head, J. W. & McKay, D. S. Ascent and eruption of a lunar high-titanium magma as inferred from the petrology of the 75001/2 drill core. *Met. Planet. Sci.* **34**, 527–540 (1999).
34. Kaufman, L. & Cohen, M. The martensitic transformation in the iron-nickel system. *J. Met.* **206**, 1393–1401 (1956).
35. Bhadeshia, H. K. D. H. *Hard bainite*. In: Solid-solid phase transformations in inorganic materials, 469-484 (The Minerals, Metals & Materials Society, Warrendale, 2005).
36. Singh, S. B. Mechanisms of bainite transformation in steels. In: Phase transformations in steels. Volume 1 - fundamentals and diffusion-controlled transformations, 385–416 (Woodhead Publishing, Philadelphia, 2012).
37. Elardo, S. M. & Shearer, C. K. Magma chamber dynamics recorded by oscillatory zoning in pyroxene and olivine phenocrysts in basaltic lunar meteorite Northwest Africa 032. *Am. Miner.* **99**, 355–368 (2014).
38. Fultz, B., Kim, J. I., Kim, Y. H. & Morris, J. W. The chemical composition of precipitated austenite in 9Ni steel. *Metall. Trans. A* **17**, 967–972 (1986).
39. Sagaradze, V. V. et al. Conditions for the violation of concentrational homogeneity of Fe–Ni Invar alloys. *Phys. Met. Metallogr.* **122**, 969–975 (2021).
40. Arioka, K., Iijima, Y. & Miyamoto, T. Rapid nickel diffusion in cold-worked carbon steel at 320-450 °C. *Philos. Mag.* **95**, 3577–3589 (2015).
41. Danilchenko, V. E., Mazanko, V. F. & Iakovlev, V. E. The effect of multiple martensitic transformations on diffusion of Fe and Ni atoms in Fe-31.7%Ni-0.06C alloy. *Nanoscale Res. Lett.* **9**, 322 (2014).
42. Dean, D. C. & Goldstein, J. I. Determination of the interdiffusion coefficients in the Fe-Ni and Fe-Ni-P systems below 900 °C. *Metall. Trans. A* **17**, 1131–1138 (1986).
43. Vasavada, A. R. et al. Lunar equatorial surface temperature and regolith properties from the diviner lunar radiometer experiment. *J. Geophys. Res. Planets* **117**, E00H18 (2012).
44. Langseth, M. G., Keihm, S. J. & Peters, K. Revised lunar heat-flow values. *Proc. Lunar Sci. Conf.* **7**, 3143–3171 (1976).
45. Hidaka, H., Sakuma, K., Nishiizumi, K. & Yoneda, S. Isotopic evidence for multi-stage cosmic-ray exposure histories of lunar meteorites: long residence on the moon and short transition to the Earth. *Astron. J.* **153**, 274 (2017).
46. Costello, E. S., Ghent, R. R. & Lucey, P. G. The mixing of lunar regolith: vital updates to a canonical model. *Icarus* **314**, 327–344 (2018).
47. Guillaume, C. E. The anomaly of nickel-steels. *Proc. Phys. Soc. Lond.* **32**, 374–404 (1919).
48. Bunshah, R. F. & Mehl, R. F. Rate of propagation of martensite. *Trans. AIME* **197**, 1251–1258 (1953).
49. Nishiyama, Z. Martensitic transformation (Academic Press, New York, 1978).
50. Olson, G. B. & Cohen, M. Principles of martensitic transformations. In: *Frontiers in Materials Technologies*, 43-87 (Elsevier, Amsterdam, 1985).
51. Yu, Z. Z. & Clapp, P. C. Growth dynamics study of the martensitic transformation in Fe-30 pct Ni Alloys: part I. Quantitative measurements of growth velocity. *Metall. Trans. A* **20**, 1601–1615 (1989).
52. Zhang, X. & Sawaguchi, T. Twinning of deformation-induced ε-martensite in Fe-30Mn-6Si shape memory alloy. *Acta Mater.* **143**, 237–247 (2018).
53. Weidner, A., Segel, C. & Biermann, H. Magnitude of shear of deformation-induced α'-martensite in high-alloy metastable steel. *Mater. Lett.* **143**, 155–158 (2015).

54. Yang, X. S., Sun, S. & Zhang, T. Y. The mechanism of bcc α′ nucleation in single hcp ε laths in the fcc γ → hcp ε → bcc α′ martensitic phase transformation. *Acta Mater.* **95**, 264–273 (2015).
55. Kim, H. J., Kim, Y. H. & Morris, J. W. Thermal mechanisms of grain and packet refinement in a lath martensitic steel. *ISIJ Int.* **38**, 1277–1285 (1998).
56. Bondar, V. I. & Danilchenko, V. E. Influence of phase cold working on the structure and strengthening of iron-nickel single crystals. *Rep. USSR Acad. Sci.* **275**, 1408–1412 (1984).
57. Sagaradze, V. V. & Kabanova, I. G. Formation of a nanocrystalline structure during direct and reverse martensitic transformations. *Mater. Sci. Eng. A* **273-275**, 457–461 (1999).
58. Steven, W. & Haynes, A. G. The temperature of formation of martensite and bainite in low-alloy steels. *J. Iron Steel Inst.* **183**, 349–359 (1956).
59. Sano, Y., Chang, S. N., Meyers, M. A. & Nemat-Nasser, S. Identification of stress-induced nucleation sites for martensite in Fe-31.8 wt%Ni-0.02wt%C. *Acta Metall. Mater.* **40**, 413–417 (1992).
60. Thadhani, N. N. & Meyers, M. A. Kinetics of isothermal martensitic transformation. *Prog. Mater. Sci.* **30**, 1–37 (1986).
61. Yeo, R. B. G. Growth of martensite in an iron-28.8% nickel alloy. *Trans. Am. Soc. Metal.* **57**, 48–61 (1964).
62. Takeuchi, S. & Suzuki, H. On "temperature interval" in lattice transformation (II). *J. Jpn Inst. Met. B* **14**, 12–16 (1950).
63. Villa, M. Isothermal martensite formation, PhD thesis (Technical University of Denmark, Lyngby, 2013).
64. Raghavan, V. & Entwisle, A. R. Isothermal martensite kinetics in iron alloys. In: *The Physical Properties of Martensite and Bainite*, 29–37 (The Iron and Steel Institute, London, 1965).
65. Shih, C. H., Averbach, B. L. & Cohen, M. Some characteristics of the isothermal martensitic transformation. *Trans. AIME* **203**, 183–187 (1955).
66. Magee, C. L. The kinetics of martensite formation in small particles. *Metall. Trans.* **2**, 2419–2430 (1971).
67. Philibert, J. & Crussard, C. Kinetics of the martensite transformation in a hyper-eutectoid steel. *J. Iron Steel Inst.* **180**, 39–50 (1955).
68. Aikawa, Y., Terai, T. & Kakeshita, T. Grain size effect on martensitic transformation behavior in Fe-Ni invar alloys. *J. Phys. Conf. Ser.* **165**, 1–4 (2009).
69. Kakeshita, T., Katsuyama, J., Fukuda, T. & Saburi, T. Time-dependent nature of displacive transformations in Fe-Ni and Fe-Ni-Mn alloys under magnetic field and hydrostatic pressure. *Mater. Sci. Eng. A* **312**, 219–226 (2001).
70. Kakeshita, T., Saburi, T., Kindo, K. & Endo, S. Martensitic transformations in some ferrous and non-ferrous alloys under magnetic field and hydrostatic pressure. *Phase Transit.* **70**, 65–113 (1999).
71. Patel, J. R. & Cohen, M. Criterion for the action of applied stress in the martensitic transformation. *Acta Metall.* **1**, 531–538 (1953).
72. Rohde, R. W. Temperature dependence of the shock-induced reversal of martensite to austenite in an iron-nickel-carbon alloy. *Acta Metall.* **18**, 903–913 (1970).
73. Rohde, R. W., Holland, J. R. & Graham, R. A. Shock-wave-induced reverse martensitic transformation in Fe-30 pct Ni. *Trans. AIME* **242**, 2017–2019 (1968).
74. Bowden, H. G. & Kelly, P. M. The crystallography of the pressure induced phase transformations in iron alloys. *Acta Metall.* **15**, 1489–1500 (1967).
75. Loree, T. R., Warnes, R. H., Zukas, E. G. & Fowler, C. M. Polymorphism of shocked loaded Fe-Mn and Fe-Ni alloys. *Science* **153**, 1277–1278 (1966).
76. Leslie, W. C., Stevens, D. W. & Cohen, M. Deformation and transformation structures in shock-loaded iron-base alloys. In: *High-Strength Materials*, 382–435 (Wiley, New York, 1964).
77. Kolomytsev, V. I., Lobodyuk, V. A. & Savvakin, G. I. The effect of the duration of a shock impact on the martensitic transformation in iron-nickel alloys. *Metallofiz. Nov. Tekh.* **3**, 69–75 (1981).
78. Fritz, J., Greshake, A. & Fernandes, V. A. Revising the shock classification of meteorites. *Met. Planet. Sci.* **52**, 1216–1232 (2017).
79. Bowling, T. J. et al. Dwell time at high pressure of meteorites during ejection from Mars. *Icarus* **343**, 113689 (2020).
80. Warren, P. H. Lunar and Martian meteorite delivery services. *Icarus* **111**, 338–363 (1994).
81. Artemieva, N. A. & Ivanov, B. A. Launch of Martian meteorites in oblique impacts. *Icarus* **171**, 84–101 (2004).
82. Carrier, W. D., Olhoeft, G. R. & Mendell, W. Physical properties of the lunar surface. In: *Lunar sourcebook - a user's guide to the moon*, 475–594 (Cambridge University Press, Cambridge, 1991).
83. Kieffer, S. W. Impact conditions required for the formation of melt by jetting in silicates. In: *Impact and Explosion Cratering*, 751–769 (Pergamon, New York, 1977).
84. Johnson, B. C., Bowling, T. J. & Melosh, H. J. Jetting during vertical impacts of spherical projectiles. *Icarus* **238**, 13–22 (2014).
85. Melosh, H. J. Impact ejection, spallation and the origin of meteorites. *Icarus* **59**, 234–260 (1984).
86. Kurosawa, K., Okamoto, T. & Genda, H. Hydrocode modeling of the spallation process during hypervelocity impacts: Implications for the ejection of Martian meteorites. *Icarus* **301**, 219–234 (2018).
87. Shoemaker, E. M. Interpretation of lunar craters. In: *Physics and Astronomy of the Moon*, 283–359 (Academic Press, New York, 1962).
88. Elliott, J. R., Melosh, H. J. & Johnson, B. C. The role of target strength on the ejection of Martian meteorites. *Icarus* **375**, 114869 (2022).
89. Yang, C. et al. Lunar impact crater identification and age estimation with Chang'E data by deep and transfer learning. *Nat. Commun.* **11**, 6358 (2020).
90. Gladman, B. J., Burns, J. A., Duncan, M. J. & Levison, H. F. The dynamical evolution of lunar impact ejecta. *Icarus* **118**, 302–321 (1995).
91. Head, J. N. Lunar meteorite source crater size: constraints from impact simulations. *Proc. Lunar Planet. Sci. Conf.* **32**, 1768 (2001).
92. Xie, C. Interactive heat transfer simulations for everyone. *Phys. Teach.* **50**, 237–240 (2012).
93. Yeo, R. B. G. The effects of some alloying elements on the transformation of Fe-22.5 pct Ni alloys. *Trans. AIME* **227**, 884–890 (1963).
94. Martínez-Blanco, D., Gorria, P., Pérez, M. J., Blanco, J. A. & Smith, R. I. Martensite-austenite transformation in $Fe_{80}Ni_{20}$ ball-milled powder. *J. Magn. Magn. Mater.* **316**, 328–331 (2007).
95. Turcotte, D. L. & Schubert, G. *Geodynamics* (Cambridge University Press, Cambridge, 2014).
96. Fritz, J., Artemieva, N. A. & Greshake, A. Ejection of Martian meteorites. *Met. Planet. Sci.* **40**, 1393–1411 (2005).
97. Sharp, T. G. & De Carli, P. S. Shock effects in meteorites. In: *Meteorites and the early solar system II*, 653–677 (University of Arizona Press, Tucson, 2006).
98. Butler, C. P. Temperature of meteoroids in space. *Meteoritics* **3**, 59–70 (1966).
99. Mijajlovic, T., Xue, X. & Walton, E. A revised shock history for the youngest unbrecciated lunar basalt - Northwest Africa 032 and paired meteorites. *Met. Planet. Sci.* **55**, 2267–2286 (2020).
100. Stöffler, D., Hamann, C. & Metzler, K. Shock metamorphism of planetary silicate rocks and sediments: proposal for an updated classification system. *Met. Planet. Sci.* **53**, 5–49 (2018).
101. El Goresy, A. et al. Shock-induced deformation of shergottites: shock-pressures and perturbations of magmatic ages on Mars. *Geochim. Cosmochim. Acta* **101**, 233–262 (2013).
102. Nastasi, M., Mayer, J. W. & Hirvonen, J. K. Ion-solid interactions: fundamentals and applications (Cambridge University Press, Cambridge, 1996).

103. Orloff, J., Utlaut, M. & Swanson, L. High resolution focused ion beams - FIB and its applications (Springer, New York, 2003).
104. Wirth, R. Focused ion beam (FIB): a novel technology for advanced application of micro- and nanoanalysis in geosciences and applied mineralogy. *Eur. J. Mineral.* **16**, 863–876 (2004).
105. Giannuzzi, L. A. & Stevie, F. A. Introduction to focused ion beams: instrumentation, theory, techniques and practice (Springer, New York, 2005).
106. Wirth, R. Focused Ion Beam (FIB) combined with SEM and TEM: Advanced analytical tools for studies of chemical composition, microstructure and crystal structure in geomaterials on a nanometre scale. *Chem. Geol.* **261**, 217–229 (2009).
107. Stadelmann, P. A software package for electron-diffraction analysis and HREM image simulation in materials science. *Ultramicroscopy* **21**, 131–145 (1987).
108. Rauch, E. F. et al. Automated nanocrystal orientation and phase mapping in the transmission electron microscope on the basis of precession electron diffraction. *Z. Kristallogr.* **225**, 103–109 (2010).
109. Bachmann, F., Hielscher, R. & Schaeben, H. Texture analysis with MTEX - free and open source software toolbox. *Solid State Phen.* **160**, 63–68 (2010).
110. Kobler, A. & Kübel, C. Challenges in quantitative crystallographic characterization of 3D thin films by ACOM-TEM. *Ultramicroscopy* **173**, 84–94 (2017).
111. Aebersold, A. B., Alexander, T. L. & Hébert, C. Height-resolved quantification of microstructure and texture in polycrystalline thin films using TEM orientation mapping. *Ultramicroscopy* **159**, 112–123 (2015).
112. Cayron, C., Barcelo, F. & de Carlan, Y. The mechanisms of the fcc-bcc martensitic transformation revealed by pole figures. *Acta Mater.* **58**, 1395–1402 (2010).
113. Cech, R. E. & Turnbull, D. Heterogeneous nucleation of the martensite transformation. *J. Met.* **8**, 124–132 (1956).
114. Bando, Y. Characteristics of phase transformations in metallic fine particles (martensitic transformation of Fe-Ni alloys and ordering of CuAu and Cu_3Au alloys). *Trans. Jpn Inst. Met.* **5**, 135–141 (1964).
115. Easterling, K. E. & Swann, P. R. Nucleation of martensite in small particles. *Acta Metall.* **19**, 117–121 (1971).
116. Zhou, Y. H., Harmelin, M. & Bigot, J. Martensitic transformations in ultrafine Fe-Ni powders. *Mater. Sci. Eng. A* **124**, 241–249 (1990).
117. Umemoto, M. & Owen, W. S. Effects of austenitizing temperature and austenite grain size on the formation of athermal martensite in an iron-nickel and an iron-nickel-carbon alloy. *Metall. Trans.* **5**, 2041–2046 (1974).
118. Jones, F. W. & Pumphrey, W. I. Free energy and metastable states in the iron-nickel and iron-manganese systems. *J. Iron Steel Inst.* **163**, 121–131 (1949).
119. Swartzendruber, L. J., Itkin, V. P. & Alcock, C. B. The Fe-Ni (iron-nickel) system. *J. Phase Equilib.* **12**, 288–312 (1991).
120. Yang, C. W., Williams, D. B. & Goldstein, J. I. A revision of the Fe-Ni phase diagram at low temperatures (≤400 °C). *J. Phase Equilib.* **17**, 522–531 (1996).

Acknowledgements

The authors would like to express their gratitude to UNIL and EPFL for their financial support. The costs of article processing (APC) have been funded by the Swiss National Science Foundation (Grant 200021-197258 awarded to O. Müntener). Special thanks are addressed to M. Cantoni and E. Oveisi for their invaluable technical assistance during the FIB and TEM sessions, and to L.P. Baumgartner, A. El Goresy, T.J. Fagan, and B.C. Johnson for their contributions through informal meetings and fruitful email correspondence.

Author contributions

P.V. assumed primary responsibility for all aspects of the project, with a particular focus on the acquisition and post-processing of SEM and EBSD data, the interpretation of the results, and paper writing. F.N. performed the FIB and TEM-EDS work, A.B.A. collected and post-processed ACOM data, and M.R. did the EPMA analyses. C.C. provided his expertize in the field of materials science and in the utilization of the ARPGE software. All co-authors, including M.A.K., O.M., and P.G., participated in the final interpretation of the data, validated the scientific aspects, and reviewed the manuscript. The present paper did not employ any form of artificial intelligence.

Competing interests

The authors declare no competing interests.

Additional information

Supplementary information The online version contains supplementary material available at https://doi.org/10.1038/s41467-025-57652-6.

Correspondence and requests for materials should be addressed to Pierre Vonlanthen.

Peer review information *Nature Communications* thanks Shaolin Li and the other, anonymous, reviewers for their contribution to the peer review of this work. A peer review file is available.